International Journal of Heat and Mass Transfer 245 (2025) 126985

Contents lists available at ScienceDirect

International Journal of Heat and Mass Transfer

journal homepage: www.elsevier.com/locate/ijhmt

Physics informed neural networks for solving inverse thermal wave coupled boundary-value problems

Hong Tang [a], Alexander Melnikov [b,c], MingRui Liu [a], Stefano Sfarra [d], Hai Zhang [a,*], Andreas Mandelis [b,c,**]

[a] Centre of Composite Materials and Structures (CCMS), Harbin Institute of Technology, Harbin, China
[b] Center for Advanced Diffusion-Wave and Photoacoustic Technologies (CADIPT), Department of Mechanical and Industrial Engineering, University of Toronto, Toronto, Ontario M5S 3G8, Canada
[c] Institute for Advanced Non-Destructive and Non-Invasive Diagnostic Technologies (IANDIT), University of Toronto, Toronto, Ontario M5S 3G8, Canada
[d] Department of Industrial and Information Engineering and Economics (DIIIE), University of L'Aquila, L'Aquila 67100, Italy

ARTICLE INFO

Keywords:
Thermal diffusivity
Thermal wave
PINN
Boundary value problems
Inverse problem

ABSTRACT

As one of the essential parameters in thermophysical analysis, effective measurement of thermal diffusivity is necessary. This paper utilizes the Physics-Informed Neural Networks (PINN) framework to simulate the diffusion of thermal waves. The governing equations / boundary-value problem (BVP) for the thermal waves are expressed in a coupled partial differential form, derived using the method of separation of variables. The inverse problem associated with the coupled partial differential equations is solved using a dimensionless equation / BVP with a loss function that incorporates physical information. Even in the presence of experimental system errors, the neural network (NN) method introduced in this work ("new NN method") was shown to be capable of robustly solving the thermal wave inverse problem without nonlinear DC components at different spatial locations, for determining the unknown thermal diffusivity of green (unsintered) metal powder compact materials. The results indicate that the coupled partial differential equations for the amplitude and phase of thermal waves within the PINN framework represent a promising strategy for determining thermophysical parameters.

1. Introduction

The advent of powder metallurgy technology has made the mass production of complex multi-component parts more efficient [1,2]. However, excessive pressing force, improper demolding, and stress concentration in such processes can lead to manufacturing defects in green metal powder compact (GMPC) materials [3,4]. These defects can reduce the performance of the sintered products, potentially turning them to waste. Particularly in the context of rising global energy prices, economic upheaval [5], and a downturn in the powder metallurgy industry, effectively assessing the defects in a GMPC before sintering, thereby allowing them to be turned to metallic powder for recycling and re-pressing, has become a critical issue for reducing the costs of discarded sintered products and enhancing product performance. Analyzing the thermal wave (TW) field generated at the surface and propagating through the body of the sample aids in evaluating the manufacturing quality of GMPC [6,7]. In this analysis, for a known modulation angular frequency ω, the TW phase velocity $\sqrt{2\alpha\omega}$ and propagation length $\sqrt{2\alpha/\omega}$ can be defined through the thermal diffusivity α. Therefore, accurate measurement of thermal diffusivity is necessary and measurement methods can be categorized based on thermal flow characteristics into steady-state measurements and transient measurements.

Steady-state measurements involve establishing a stable temperature field within the sample to be tested, measuring the temperature gradient and the heat transfer rate per unit area, and then calculating the thermal conductivity based on Fourier's law [8,9]. The thermal diffusivity can then be obtained through the relationship between sample thermal conductivity and density. However, due to the lengthy measurement time, thermal losses significantly affect the accuracy of thermal diffusivity measurements. Thermal diffusivity is typically measured directly due to advancements in transient thermal conduction theory. Transient

* Corresponding author.
** Corresponding author at: Center for Advanced Diffusion-Wave and Photoacoustic Technologies (CADIPT), Department of Mechanical and Industrial Engineering, University of Toronto, Toronto, Ontario M5S 3G8, Canada.
E-mail addresses: hai.zhang@hit.edu.cn (H. Zhang), mandelis@mie.utoronto.ca (A. Mandelis).

https://doi.org/10.1016/j.ijheatmasstransfer.2025.126985
Received 6 November 2024; Received in revised form 9 March 2025; Accepted 15 March 2025
Available online 26 March 2025

measurements can be categorized into pulsed and periodic methods based on the excitation approach. The pulsed method minimizes the impact of thermal losses during measurement by detecting relative temperature changes in a small sample over a short duration, thereby enhancing measurement accuracy [10,11]. However, for materials with high thermal diffusivity, the rapid temperature response can lead to significant measurement inaccuracies due to the delay effects of the measurement system. The periodic method utilizes an infrared thermography system to detect TWs excited by periodic thermal sources, measuring thermal diffusivity through the amplitude decay and phase lag of the TW response. This method reduces the demands on the measurement system's response speed by leveraging the average characteristics of periodic thermal responses [12,13]. Lock-in demodulation is a common TW response analysis method in periodic measurements. Additionally, some research indicates that heat loss should be taken into account when measuring thermophysical parameters in periodic measurements.

Ozisik [14] has shown that BVPs for diffusing thermal fields align with traditional heat conduction theory, where the application of third-kind boundary conditions always involves heat loss through solid boundaries, with the cooling coefficient often treated as a constant independent of temperature or space [15]. Similarly, He [16] assumed a constant cooling coefficient in the theoretical thermal analysis of microelectronic devices, whereas Mandelis et al., [17,18] adopted the same assumption while addressing the structure and non-reflective/non-refractive properties of parabolic differential equations for TWs. However, earlier research has shown that assuming a constant cooling coefficient is ineffective for solids with large surfaces, as they are significantly affected by the amplitude of modulated TW fields with substantial spatial variations, particularly those related to TW depth profiles. To address this issue, a variable cooling coefficient-related power series solution has been proposed for measuring thermal diffusivity. Nevertheless, representing the cooling coefficient using combined power series leads to complex expressions that reduce the solvability of the analysis and complicate the physical interpretation and signal processing, especially for higher-order power series. Furthermore, the multiple orders of magnitude of thermophysical property values involved in the associated BVPs create additional computational errors due to the multi-scale nature of the problem.

In this study, we focus on the application of physics-informed neural networks (PINNs) to solve the boundary value problem of TWs under third-kind boundary conditions, with a particular emphasis on the thermophysical analysis of GMPC. Unlike conventional data-driven approaches, such as neural networks (NNs) [19,20] and genetic algorithms [21], which rely solely on experimental data and may lack physical consistency, PINNs have emerged as a powerful tool for solving partial differential equations and inverse problems. By incorporating physical laws directly into the NN training process, PINNs constrain the solution space to physically meaningful results, significantly improving accuracy and robustness [22,23]. This approach overcomes the limitations of traditional NNs, such as their reliance on large datasets and lack of physical interpretability, while also providing a more efficient alternative to computationally expensive genetic algorithms that struggle with multi-scale problems. Furthermore, unlike finite element and finite difference methods, which require domain discretization and may face challenges in handling complex geometries, PINNs offer a meshless framework that seamlessly integrates physics and data, making them particularly well-suited for addressing the challenges of multi-scale thermal analysis in GMPCs. Recent studies have highlighted the effectiveness of PINNs in addressing complex thermal problems, including inverse heat transfer and thermal diffusivity estimation [24,25]. However, it is noteworthy that, as a meshless numerical method, applying PINNs directly to analyze dynamic TW fields (which include both steady-state and unsteady processes) can incur significant computational costs and risk non-convergence of training results. To address these challenges, we propose a novel approach that combines PINNs with the method of separation of variables to analyze steady-state TW fields. This approach not only circumvents the computational challenges associated with dynamic TW fields but also enhances the robustness and efficiency of the analysis. Specifically, our work addresses the limitations of traditional methods by introducing a dimensionless BVP framework for the PINN loss function, which mitigates the effects of multi-scale thermophysical coefficients. Additionally, we propose a method for filtering the DC component of TWs, further improving the accuracy of thermal diffusivity measurements.

The main contributions of this paper are as follows: 1) Casting of the BVP for the steady-state amplitude and phase of a dynamic TW field with a spatially variant side surface cooling coefficient, reducing computational costs and improving convergence; 2) Application of PINNs to solve the TW BVP problem with third-kind boundary conditions and address the inverse problem of thermal diffusivity measurement in GMPC; 3) Setting up a dimensionless BVP framework for the PINN loss function, utilized to mitigate the effects of multiple orders-of-magnitude (multi-scale) thermophysical coefficient values; 4) Presenting a method for filtering the DC component of TWs in thermal diffusivity measurement and considering the impact of computational errors and experimental system errors on the measurement results. These innovations enable us to achieve higher precision in thermal analysis while maintaining computational efficiency, making our approach particularly valuable for the thermophysical characterization of GMPCs.

The study is organized as follows. In Section 2, partial differential equations for the amplitude and phase of steady-state TWs related to variable cooling coefficients are established within the PINN framework. In Section 3, a method for filtering out nonlinear DC components of TWs is proposed. Then in Section 4, the signal-to-noise ratio (SNR) of transient thermal response in the time-frequency domain is analyzed, and based on the AC component of TWs, the thermal diffusivity of GMPC is measured using PINNs. Additionally, measurement errors in the experimental system have been considered. Finally, Section 5 summarizes the conclusions.

2. Establishment of the thermal-wave model and solution using PINN

This section first establishes a spatially dependent TW field related to variable cooling coefficients based on third-kind boundary conditions of the TW boundary value problem. Then the TW partial differential equations are analyzed within the PINN framework and the experimental TW responses are used to infer the thermal diffusivity.

2.1. Establishment of the thermal wave model with spatially dependent cooling coefficients

Through the photothermal conversion effect, an opaque rectangular solid is periodically heated by a sinusoidally modulated laser beam with an angular frequency ω. The heated spot is rectangular, and the energy is uniformly distributed over the incident surface. This temperature fluctuation induced by the periodic heat source is referred to as a TW, represented as $T(x,t) = A(x)\sin[(\omega t + \phi(x))]$, where x is the spatial coordinate, t is time; A and ϕ represent the amplitude and phase, respectively. The cooling coefficient of the side walls can be considered as a spatially dependent function $h(x)$ [26]. In the absence of convergence and other sources within the infinitesimal segment, the following energy equation can be derived based on the conservation of thermal power:

$$\frac{\partial^2 \Delta T(x,t)}{\partial x^2} - \frac{1}{\alpha}\frac{\partial \Delta T(x,t)}{\partial t} - \left(\frac{R}{Sk}\right)h(x)\Delta T(x,t) = 0, x \in \Omega \tag{1}$$

where α is the thermal diffusivity, R is the perimeter of the cross-section satisfying $R = 2(\mathrm{L} + \mathrm{B})$, S is the cross-sectional area satisfying $S = \mathrm{L} \times \mathrm{B}$, where L and B are the height and width of the sample, respectively; k is the thermal conductivity.

To ensure the convergence of TWs in numerical calculations, directly analyzing the amplitude and phase of steady-state TWs is an effective approach. Substituting $A(x)\sin[(\omega t+\phi(x))]$ into Eq. (1) and separating the amplitude and phase, the following governing equations can be obtained:

$$\frac{d^2A}{dx^2}-A\left(\frac{d\phi}{dx}\right)^2-Eh(x)A=0 \tag{2a}$$

$$A\frac{d^2\phi}{dx^2}+2\frac{dA}{dx}\frac{d\phi}{dx}-A\frac{\omega}{\alpha}=0,\ x\in\Omega \tag{2b}$$

where $E=R/Sk$ and Ω is the volume of the domain. The boundary conditions corresponding to Eq. (2) are:

$$-k\frac{dA}{dx}\bigg|_{x=0}=q\cos(\phi-\phi_s)-hA \tag{3a}$$

$$kA.\frac{d\phi}{dx}\bigg|_{x=0}=q\sin(\phi-\phi_s) \tag{3b}$$

where q is the heat flux satisfying $q=I_0/S$, where I_0 is the heat source power; ϕ_s is the phase of the incident excitation waveform.

2.2. Analysis and measurement of thermal wave partial differential equations within the PINN framework

The NNs are the core of PINNs, in which the input x is iteratively mapped through hidden layers to the outputs A and ϕ. In each layer, this mapping process is accomplished through a combination of hyperparameters θ (weights and biases) and linear or nonlinear activation functions. The input signal first undergoes a linear combination in the neurons, i.e., multiplied by the corresponding weights and a bias term is added. Subsequently, the combined result is processed through the activation function, introducing nonlinearity. This allows the NNs to capture the complex nonlinear relationships between inputs and outputs [27,28].

The amplitude, phase, and spatial heat loss coefficient can be approximated using NNs, i.e., $NN_A\approx A$, $NN_\phi\approx\phi$, and $NN_h\approx h$. The gradients of amplitude and phase in the PINN framework can be efficiently computed using automatic differentiation [29]. To train the NNs, a training set consisting of points from spatial boundaries Γ and volume domains Ω is required. The training points configured on Γ and Ω are 1 and N_p, respectively. To approximate A and ϕ, the loss function containing the physical model should be minimized. The loss function has been incorporated in Eq. (2) with boundary conditions (3). For forward problems, no additional data are required in the loss function. The loss function L is defined as follows:

$$L(\theta)=L_{p1}(\theta)+L_{p2}(\theta)+L_{Ab}(\theta)+L_{\phi b}(\theta) \tag{4}$$

where the individual PINN loss functions can be expressed as

$$L_{p1}(\theta)=\min_\theta\left\{\frac{1}{N_{p1}}\sum_i^{N_{p1}}\left\|\left[\frac{d^2NN_A}{dx^2}-NN_A\cdot\left(\frac{dNN_\phi}{dx}\right)^2-E\cdot NN_h\cdot NN_A\right](x_i;\theta)\right\|^2\right\} \tag{5a}$$

$$L_{p2}(\theta)=\min_\theta\left\{\frac{1}{N_{p2}}\sum_i^{N_{p2}}\left\|\left[NN_A\cdot\frac{d^2NN_\phi}{dx^2}+2\frac{dNN_A}{dx}\frac{dNN_\phi}{dx}-\frac{\omega}{\alpha}NN_A\right](x_i;\theta)\right\|^2\right\} \tag{5b}$$

$$L_{Ab}(\theta)=\min_\theta\left\{\frac{1}{2}\left\|k\frac{dNN_A(0;\theta)}{dx}+q\cos\left(NN_\phi(0;\theta)\right)-NN_h(0;\theta)\cdot NN_A(0;\theta)\right\|^2\right\} \tag{5c}$$

$$L_{\phi b}(\theta)=\min_\theta\left\{\frac{1}{2}\left\|k\cdot NN_A(0;\theta)\frac{dNN_\phi(0;\theta)}{dx}-q\sin\left(NN_\phi(0;\theta)\right)\right\|^2\right\} \tag{5d}$$

where $x_i\in\Omega$. Minimizing this loss function using an appropriate optimization algorithm can yield the optimal parameter θ for the NNs.

The inverse problem defined by treating the thermal diffusivity, α, as a learnable parameter can be addressed by adding a parameter term to the parameter update of backpropagation, highlighting the significant advantage of PINNs over traditional linear solvers. The training points x_{data} are selected firstly in the spatial domain $\Omega\cup\Gamma$ and include the experimental amplitude A_{data} and experimental phase ϕ_{data}. Then, based on Eq. (4), a feedforward NN with input x and outputs A and ϕ is constructed. Finally, the loss function defined below is minimized using an optimization algorithm, aiming to find the optimal parameters that approximate the true thermal diffusivity $\bar{\alpha}$ of the experimental sample:

$$L_R(\theta)=\min_\theta\left\{\left\{L(\theta)+\frac{1}{N_{data}}\sum_{i=1}^{N_{data}}\left[\|A_{data}-A\|^2+\|\phi_{data}-\phi\|^2\right](x_i;\theta)\right\},\ x_i\in\Omega\cup\Gamma\right\} \tag{6}$$

where A_{data} and ϕ_{data} represent the experimental data available for the inverse problem at the point N_{data}. The prediction of thermal diffusivity requires the inclusion of additional information in the loss function, as illustrated in Fig. 1. In the study of inverse operations, the Jacobian matrix of the NNs must have a non-zero determinant, be invertible, and maintain a reasonable ratio between its maximum and minimum eigenvalues to ensure the uniqueness of the solution and the stability of the computation. The algorithm for the inverse problem follows the same principles as the forward problem, with minor modifications to the loss function [30]. In addition to the outputs A and ϕ, PINNs can now predict unknown thermal physical parameters or initial or boundary conditions in thermal physical modeling by utilizing known

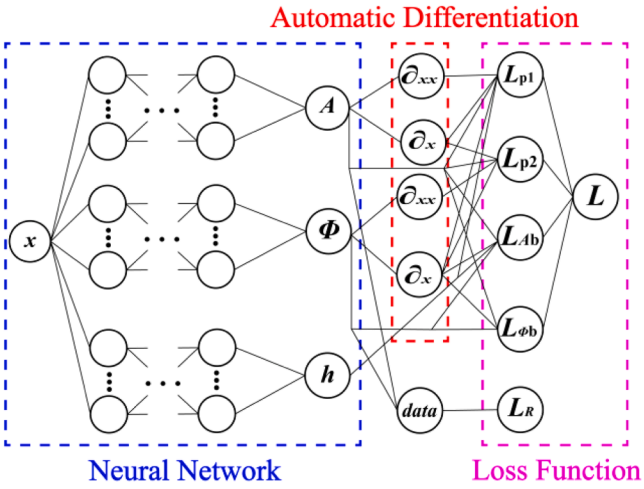

Fig. 1. The structure of the NN and automatic differentiation for loss function optimization. The left side shows the input, hidden layers, and output of the neural network. The automatic differentiation module (red box in the middle) computes partial derivatives, which are used for the combined optimization of multiple loss functions (pink box on the right). For inverse problems, the PDEs are supplemented with experimental data.

experimental data.

3. Filtering method for DC components in experimental thermal response

The experimental amplitude value A and phase value ϕ can be obtained using lock-in thermography (LIT) for the NN study [31,32]. It is important to note that the TW signal $T(i,j,t)$ in the experiment is a combination of both DC and AC signals, where i and j are pixel indices. The nonlinear characteristics of the DC signal can influence the calculations of A and ϕ through LIT [20]. The wavelet decomposition is considered to avoid the above problem [33,34]. The wavelet decomposition for removing the nonlinear DC signal from the TW can be expressed as follows:

$$a_m(n) = \sum_k T(i,j,k)\cdot\delta(2n-k),\ m = 0,1,\ldots,N-1 \tag{7a}$$

$$b_m(n) = \sum_k T(i,j,k)\cdot\theta(2n-k),\ m = 0,1,\ldots,N-1 \tag{7b}$$

where $a_m(n)$ and $b_m(n)$ represent the approximation coefficients and detail coefficients of the TW at the m-th decomposition level, respectively. $\delta(2n-k)$ and $\theta(2n-k)$ represent low-pass and high-pass filters. $a_m(n)$ represents the low-frequency components of the TW signal, reflecting its overall trend. Conversely, $b_m(n)$ represents the high-frequency components of the TW, capturing the details and abrupt changes present within it. The total number of decomposition levels is denoted as N, with the maximum value of N satisfying $N = \log_2(L_s)$, where L_s represents the duration of the TW signal. For TW responses under square wave modulation, which inherently contain multiple frequency components (broadband signal), increasing the value of N allows for better capture of the long-term drift or slow fluctuations in the TW response. The relationship between the sample number n and the decomposition level m is expressed as $n_m = n/2^m$. Additionally, the relationship between the discrete time k and continuous time t is represented as $t = k/f_s$, where f_s is the sampling frame rate of the infrared thermal imager.

The high-pass filter θ is constructed from the coefficients of the low-pass filter δ by mirroring and alternating the signs, satisfying the following expression:

$$\theta_m(n) = (-1)^m\delta(N-1-m) \tag{8}$$

The coefficients of Symlet 4 wavelets are utilized in Eq. (8) [35]. The nonlinear DC signals can be filtered from the TW signal by combining the decomposed approximation coefficients $a_m(n)$ and detail coefficients $b_m(n)$ based on the following expression,

$$\overline{T}(i,j,t) = \sum_m [a_m(n)\cdot\delta(2n-k) + b_m(n)\cdot\theta(2n-k)],\ m \neq 0 \tag{9}$$

4. Experiment and discussion

This section first presents the experimental setup used for sampling. The SNR of the instantaneous thermal response under periodic heating and the influence of nonlinear DC were analyzed. Then, the measurement of thermal diffusivity for GMPC is processed using the PINNs based on dimensional partial differential equations. Additionally, the thermal diffusivity of GMPC is measured using dimensionless partial differential equations. Finally, the impact of experimental system errors on the measurement results is discussed.

4.1. Experimental setup and sample

The experimental setup was established for data acquisition and is shown along with the sample configuration in Fig. 2. The system includes a laser and driver, a mid-infrared camera, a signal generator and a computer. An F22SMA-B 808-nm continuous laser served as the heat source for heating the specimen. The FLIR A6751 mid-infrared camera was controlled via FLIR ResearchIR Max software. A dual-channel Agilent 33500B signal generator was used to drive the laser, with one channel connected to the laser diode and the other used for triggering the mid-infrared camera. The sample was the GMPC material and the length, depth (thickness), and width were 31 mm, 12 mm, and 6 mm, respectively. System stability was examined and was found that fluctuations in laser emission could introduce random errors in the measurements affecting the amplitude and phase measurements, thereby reducing the reliability of the calculated thermal diffusivity. The camera's sampling interval was another source of random error that could affect measurement accuracy as insufficient sampling rates might lead to insufficient numbers of data points for accurate phase reconstruction, thus also influencing the thermal diffusivity estimation. Considering these factors, close attention was paid to the experimental setup, calibration, and data processing routines to ensure the reliability of thermal diffusivity measurements and minimize uncertainties in the results.

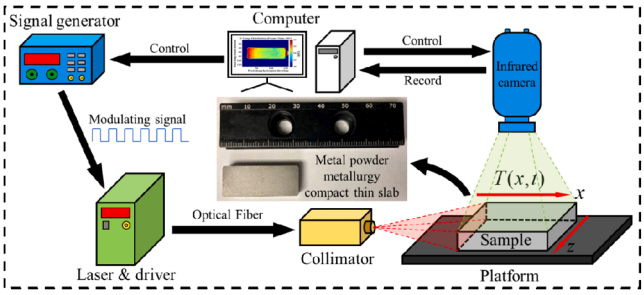

Fig. 2. Schematic diagram of a temperature field measurement system for GMPC based on laser modulation and infrared measurement. The system consists of a signal generator, laser driver, optical fiber, collimator, and infrared camera, with the computer controlling and recording the temperature changes over time.

A square-wave optical excitation signal was used as the modulation waveform with 50 % duty cycle as it exhibits a better SNR than a pure sine wave [36]. The laser diode was operated at a power of 5 W. A homemade window was inserted to ensure the laser beam uniformly irradiated the side (cross-sectional) surface of the sample. The sampling rate of the modulation signal was set at 10,240 Hz, and the data were stored on a data acquisition card used for characterizing the GMPC.

4.2. Modulated thermal response under periodic heating

A comparison of the SNR for the modulated thermal response in the time-frequency domain under periodic heating was conducted. The modulation frequency of the laser beam was set at 0.02 Hz. The sample was periodically heated over 2000 s, i.e., 40 cycles. The sampling frame rate of the mid-infrared camera was 1 Hz, with a pixel window of 128 × 160. The instantaneous modulated thermal response distributions over the mid-infrared (MIR) camera's viewing area (the entire side area of the sample) are shown in Figs. 3(a) and (b), respectively, at instants 848 and 861. The MIR camera-detected temperature of the holder (right end) is not related to the sample but is due to the higher emissivity of the holder, therefore, any impact of this effect on the experimental results could be ignored. Furthermore, locations were marked every 7 mm from the illumination side (left side) to analyze the influence of noise on the instantaneous thermal response, as shown in Fig. 3(a), where the distance between P1 and P5 was 28 mm. The distributions of thermal responses at instants 848 and 861 across positions P1 to P5 are shown in Figs. 3(c) and (d).

The value of the instantaneous thermal response decreased exponentially with distance from the irradiated upper surface due to the thermal diffusion, as shown in Fig. 3. It should be noted that such transient thermal responses [37,38] over the depth coordinate produce

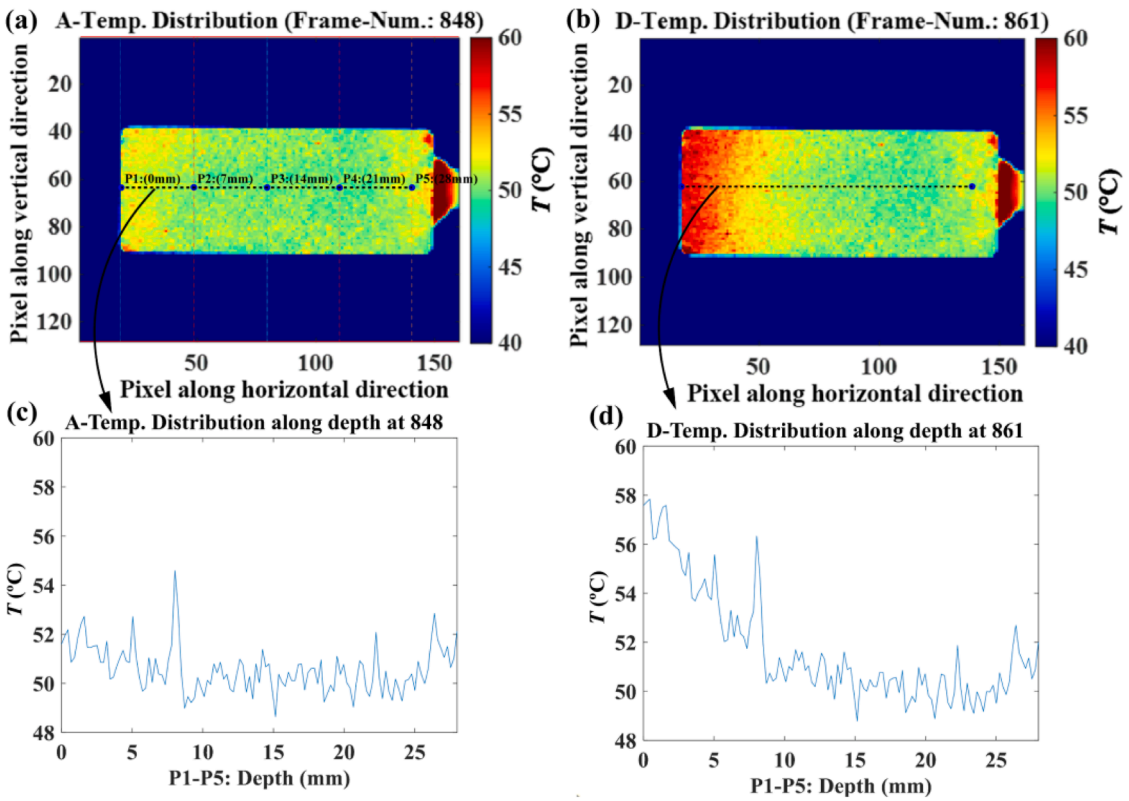

Fig. 3. Temperature distribution and temperature variation curves along the depth direction of the GMPC at different frame numbers. Instantaneous modulated responses at (a) moment 848 and (b) moment 861 over the entire side / depth coordinate instantaneous responses at (c) moment 848 and (d) moment 861 along positions P1 to P5.

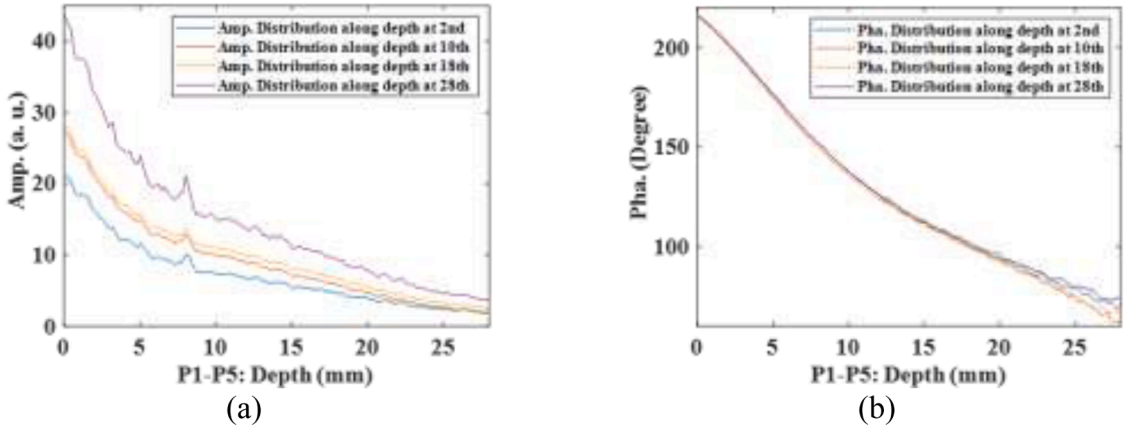

Fig. 4. The horizontal variation trend of amplitude and phase along the positions P1 to P5: (a) amplitude, (b) phase.

significant noise which limits measurement precision. The increasing traces above 25 mm as the increases are solely attributed to the backing emissivity. The TW amplitude and phase distributed along the depth coordinate in the 2nd, 10th, 18th, and 28th cycle were measured using the lock-in method. The changes in amplitude and phase over the horizontal direction from P1 to P5 and over different cycles are shown in Fig. 4. For a fixed cycle, in Fig. 4(a) amplitude values exhibited exponential decay with increasing distance, as expected. In Fig. 4(b), phase delay gradually increased with distance but was almost unaffected by the number of cycles, as expected. For depth beyond 15 mm from the optically heated surface, phase delay fluctuated with increasing cycle numbers due to the TW exceeding twice the thermal diffusion length, significantly worsening the SNR.

4.3. Effect of modulation period and frame rate drop on the measurement of thermal waves without DC

The above-mentioned experimental analysis indicates that noise limits the applicability of transient thermal responses. To better characterize the GMPC, the frequency-domain amplitude and phase of TW were considered. The GMPC was placed in an approximately stationary environment in air. For the 0.02 Hz square wave modulation signal, the frame rate of the mid-infrared camera was adjusted to 15 Hz for improving sampling accuracy, while other parameters remained unchanged. The nonlinear DC component influences the values of LIT amplitude and phase. The DC component of the TW signal over six modulation periods was removed using linear methods, parabolic

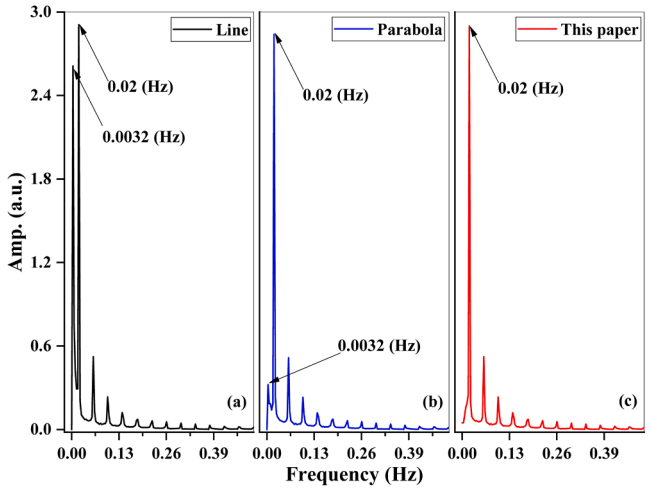

Fig. 5. The amplitude spectra of the Fourier transform for the TW signals after the removal of the DC component using the line, parabola, and NN method; (a) line, (b) parabola, (c) the method of this paper.

methods, and the new NN method. Subsequently, the amplitude spectra of Fourier transform for the TW signals after the removal of the DC component using different methods were calculated as shown in Fig. 5.

In Fig. 5, Frequencies above the fundamental frequency are harmonics due to the use of a modulated 50 % duty-cycle square wave. In this case, the odd harmonic components with different amplitudes were simultaneously transmitted into the GMPC. It should be noted that the amplitude spectrum obtained using the new NN method does not exhibit any spurious frequencies below the fundamental frequency compared to the amplitude spectra from linear and parabolic methods. These spurious frequencies cannot be filtered out through the low-pass filtering process in LIT. It was observed that as the number of modulation cycles decreases to six, the SNR of the amplitude and phase along the depth distribution significantly declines. This is because the deposited energy density increases with the number of cycles and indicates that the SNR improves with an increasing number of modulation cycles. However, no significant changes in SNR are observed with a further increase in the number of modulation cycles. Furthermore, for the new NN method modulation signal with a sampling rate of 10,240 Hz, the total number of frames captured by the camera for thermal response was 4546. The total number of usable frames for thermal response was 3971 after synchronization between the modulation signal and the thermal response. As the modulation signal sampling rate decreased, experimental results showed a marked decline in the total number of usable frames in the thermal response (frame dropping), leading to a reduction in the SNR of the amplitude and phase signals. This behavior can be explained by considering that the discarded frames introduce noise relative to the original signal, thereby decreasing the accuracy of signal reconstruction. Similar experimental results were observed with reduced camera sampling rates, despite satisfying the Nyquist sampling criterion.

4.4. Thermal diffusivity measurements under dimensional PDEs

The PINN was trained to fit the experimental amplitude and phase values and predict the thermal diffusivity of GMPC. The number of hidden layers was eight in the NNs with 64 neurons in each layer. The Xavier initialization method was employed to initialize the network parameters [39]. Both the hidden and output layers utilized the hyperbolic tangent (tanh) activation function [40]. The Adam optimization algorithm [41] was used to update the network parameters based on gradient descent, in which an initial learning rate was 10^{-3} with a decay of 0.1 every 100 iterations. The loss function was computed at arbitrary locations within the model domain, referred to as collocation points. The range of collocation points was set to be consistent with points P1 to P5. The batch size was set to 256 in the Ω domain and 1 at the boundaries. The length, width, and height of the GMPC were 3.1×10^{-2} m, 6×10^{-3} m, and 1.2×10^{-2} m, respectively. The output power of the laser was 5 W. The computational parameter values for the problem were $R = 3.6 \times 10^{-2}$ m, $S = 7.2 \times 10^{-5}$ m^2, $q = 1.736 \times 10^5$ W/m^2. The thermal conductivity k is 83 W/m·K [42].

The PINN training was iterated until the training loss was less than 10^{-6} to meet the convergence criterion. A total of 20,000 epochs were executed, but the optimizer did not converge to the preset training loss value; instead, it achieved a significant training loss of 10^9. Additionally, the results indicated that the optimizer got stuck at a local minimum. Therefore, even increasing the number of neurons within the same neural network configuration did not reduce the training loss value. The large training loss was attributed to the presence of multi-scale coefficient values in the PDEs. The differing orders of magnitude in the values of these multi-scale coefficients, caused by varying measurement units, result in large computational errors. This makes it difficult for PINNs based on dimensional PDEs to converge to smaller training loss values. Therefore, it became necessary to convert the dimensional form of the PDEs into a dimensionless form.

4.5. The analysis of the non-dimensional TW BVPs using PINN

{1.5} Based on the PINN framework from the previous section, the performance of the dimensionless PDEs and the associated BVPs was tested and evaluated. The variables and parameters could be kept within specific ranges by nondimensionalizing, thereby enhancing the performance and generalization of the NNs. Additionally, the dimensionless PDEs generate more interpretable solutions by eliminating measurement units,making it easier to understand the underlying physical phenomena and compare results across different physical systems in terms of ratios and parameters. The Eqs. (2) and (3) were non-dimensionalized and the following characteristic quantities were defined: $L_0 \equiv \sqrt{2\alpha/\omega}$,$A_0 \equiv \frac{q}{k}L_0$, $H_0 \equiv \frac{h}{k}L_0$. The dimensionless expressions for the governing Eq. (2) and boundary condition Eq. (3) can then be written as:

$$\frac{d^2\overline{A}}{dX^2} - \overline{A}\left(\frac{d\phi}{dX}\right)^2 - EH(X)\overline{A} = 0,\ \overline{A}\frac{d^2\phi}{dX^2} + 2\frac{d\overline{A}}{dX}\frac{d\phi}{dX} - 2\overline{A} = 0 \tag{10}$$

$$-\frac{d\overline{A}}{dX}\bigg|_{X=0} = \cos(\phi - \phi_s) - H_0\overline{A},\ \overline{A}.\frac{d\phi}{dX}\bigg|_{X=0} = \sin(\phi - \phi_s) \tag{11}$$

where $X = x/L_0$, $\overline{A} = A/A_0$. The same NNs architecture used in Eq. (5) was employed to solve this dimensionless set of equations and boundary conditions (BVPs) to fit the parameters. It should be noted that there were fluctuations in the values of TW amplitude and phase along the vertical direction, particularly for amplitude, as shown in Fig. 4. This variability was attributed to factors such as the smoothness of the

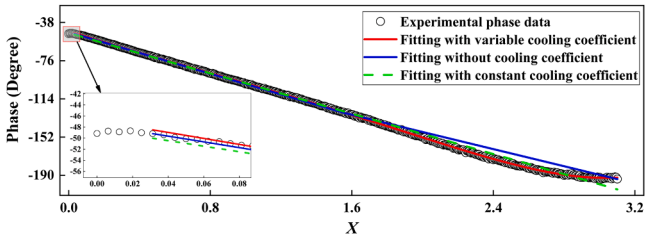

Fig. 6. Comparison of fitting models with different cooling coefficients against experimental phase data. Includes experimental phase data (black circles), fitting with variable cooling coefficient (red solid line), fitting without cooling coefficient (blue solid line), and fitting with constant cooling coefficient (green dashed line).

material surface and the configuration of the heat source during the experiment, which could affect the amplitude measurements more significantly than the phase measurements. Then, the phase results were used for measuring the thermal diffusivity of the sample while the amplitude-based results were discarded.

The phase depth distribution data of the experimental TW field from P1 to P5 is shown in Fig. 6. To avoid overfitting, the number of training points was gradually increased until the model's performance became satisfactory.

The phase depth distribution data of the experimental TWs field are nonlinear, as shown in Fig. 6. The phase distribution of theoretical TWs along depth was linear if the cooling coefficient was not considered in the control equation or if a constant cooling coefficient was considered. This oversight can lead to significant measurement errors in the thermal diffusivity values. Notably, the first five data points in the experimental TW field (next to the laser incidence surface) do not exhibit phase delays along their corresponding depths. This may be due to one or more of the following reasons: 1) these depths are within the energy deposition range of the laser, resulting in a distributed thermal energy source. 2) The position near the heat source may be influenced by source superposed boundary conditions, such as surface heat dissipation and uneven heat source distribution. This could cause irregularities in the heat flow direction and distribution near the heat source, thereby masking the expected phase delay effect. 3) The actual heat source may not be an ideal line-shaped source. If the heat source exhibits diffusion, the area near the heat source would be affected by heat dissipating in multiple directions, leading to the emergence of higher dimensional effects that can affect the phase delay. Consequently, these first five data points were excluded from the fitting process for thermal diffusivity.

The experimental phase data aligned closely with the theoretical values in Fig. 6, when the residual of the PINN loss function with a variable cooling coefficient was $<10^{-6}$. Furthermore, based on the best fit results, the measured thermal diffusivity was found to be 6.28×10^{-6} m^2/s. Each time the PINNs were run, different thermal diffusivity values were fitted due to the optimizer converging at various local minima. This variability allowed for the identification of the fluctuation range of the inverse problem solution through multiple runs of PINNs. The fluctuation range of the measured thermal diffusivity was approximately 3 % after numerous iterations. Additionally, translating P1-P5 vertically revealed that the fluctuation range of the measured thermal diffusivity was only 1 %, indicating that the new NN method was insensitive to the spatial location of the measurements. **{1.2}** The tailored design of our PINN architecture has demonstrated significant advantages in addressing the complexity of thermal wave problems. Unlike traditional methods such as finite element and finite difference methods, which struggle with multi-scale coefficients and dynamic fields, our approach leverages the meshless nature of PINNs and the embedding of physical laws to achieve high accuracy and computational efficiency. The dimensionless formulation of the BVPs has proven particularly effective in mitigating the effects of multi-scale thermophysical coefficients, while the separation of variables has allowed us to focus on the steady-state component of the TWs field, reducing computational costs and improving convergence. These design choices collectively enable our PINN architecture to outperform traditional methods in both accuracy and efficiency, making it a powerful tool for the thermophysical characterization of GMPC.

Although the GMPC was placed in an approximately stationary environment in air, natural convection and radiative heat transfer were inevitably present in the experiment. A series of cooling coefficients, represented by pixel strings along the depth profile at different vertical positions, is shown in Fig. 7.

In Fig. 7, most variations in the cooling coefficient occur in the depth direction, with only minor changes observed in the vertical direction, suggesting that the test sample was essentially uniform in the vertical dimension. To analyze the impact of different frequencies on the measurement results, modulation frequencies of 0.01 Hz and 0.05 Hz were

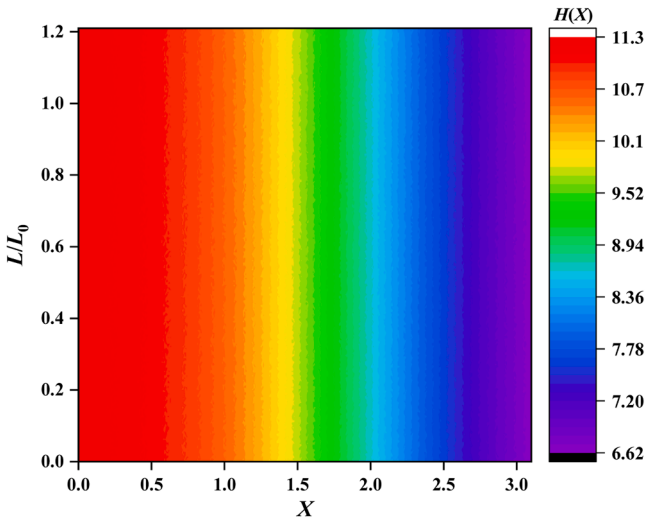

Fig. 7. The distributions of cooling coefficients over the camera viewing plane.

considered, corresponding to frame rates of 7.5 Hz and 30 Hz, respectively. All other parameters remained fixed, and the measurement process was similar to that used for the 0.02 Hz frequency. The measured thermal diffusivity values at 0.01 Hz and 0.05 Hz were 4.77×10^{-6} m^2/s and 7.13×10^{-6} m^2/s, respectively. It is evident that the thermal diffusivity values measured at different excitation frequencies vary significantly. This may be due to the combined effects of any heterogeneous regions in the GMPC, boundary cooling effects, deviations from ideal thermal conduction models, and equipment limitations. To obtain an accurate thermal diffusivity value, it is typically necessary to perform a comprehensive analysis of the measurements across various frequencies. Combining the measurement results from the three modulation frequencies, the average measured thermal diffusivity was found to be 6.06×10^{-6} m^2/s, with a fluctuation range of 1 % to 3 %. The average value compared favorably with similar metal powder compacts reported by Rombouts et al., 3.75×10^{-6} m^2/s [43], and fell within the same numerical range as the GMPC made from water atomized, iron powder ASC100, and pre-alloyed steel powders Astaloy Mo and Astaloy CrM [44]. The differences in the predicted thermal diffusivity values may be attributed to variations in the density of the test samples.

4.6. Impact of experimental factors on thermal diffusivity measurement precision

In addition to the aforementioned computational errors, several experimental factors, such as imaging ratio, temperature resolution, and laser energy stability, significantly influence the accuracy of thermal diffusivity measurements [45]. The scale of the measurement ruler captured by the infrared camera is affected by the imaging ratio. A stainless-steel ruler was used in this study, which has a higher emissivity at the scale lines compared to other areas of the ruler. Clear images of the ruler could be formed through precise focusing within the appropriate radiation temperature range. For the camera's pixel density of 640×512, the imaging ratio factors were 14 steps per millimeter in the horizontal direction and 16 steps per millimeter in the vertical direction. Notably, differences in sensitivity and scanning time among the sensors in the vertical direction made it difficult to accurately determine the vertical imaging ratio. Therefore, the horizontal imaging ratio was adopted. After multiple readings in the horizontal direction, a measurement error of 0.05 steps per millimeter was found, which equates to 5 %. Consequently, the overall fluctuation in thermal diffusivity measurements due to the imaging ratio factor and computational errors was estimated to be between 1 % and 3.7 %. The influence of the camera's temperature resolution was minimal since the measurement of thermal

diffusivity was based on phase data and variations in temperature resolution have a limited impact on the phase readings, thereby resulting in a negligible effect on the thermal diffusivity measurement.

5. Conclusions

The analysis of TWs is challenging due to the non-steady state and multi-scale interactions present in periodic transient thermal responses. This study aimed to predict thermal diffusivity values by solving the amplitude-phase coupled control PDEs and associated BVPs governing dynamic (modulated) steady-state TWs. Recently, PINN has emerged as an effective method for solving PDEs. The PINN algorithm and non-dimensionalization steps were employed in this new NN study to facilitate the learning process of TW diffusion. The PINN framework successfully addressed the inverse problem of the non-dimensionalized amplitude-phase coupled control PDEs/BVPs, leading to the following findings:

(1) Comparing the SNR of samples characterized by DC and AC components showed that characterization of the AC component was more reliable. It was crucial to effectively filter out the nonlinear DC components to avoid the emergence of spurious frequencies below the fundamental frequency in the calculation of TW amplitude and phase. Furthermore, increasing the number of modulation periods and reducing the frame rate drop could enhance the SNR of amplitude and phase signals.
(2) The ability of the PINN to accurately reveal unknown thermal diffusivity parameters through its inverse problem-solving capabilities has been demonstrated. The proposed algorithm successfully learned the thermal diffusivity parameters of GMPC under periodic heating, with a fluctuation range of <3.7 %. The effectiveness of this algorithm in solving the inverse problem was validated by comparing it with reported parameter values of similar materials. In cases of the inverse problem, even when utilizing experimental data from different spatial locations during the learning process, the fluctuation range of the predicted results was <1 %, indicating that the new NN algorithm is both accurate and robust across various measurement locations.
(3) while experimental system errors were not directly incorporated into the training of the NNs, they still contributed to the computational results with an interference error of <0.7 %.

In summary, non-dimensional TW PDEs/BVPs within the PINN framework can efficiently, robustly, and adaptively simulate diffusion processes at the dynamic steady state. In future, this approach could be extended to estimate the physical parameters of various diffusion waves in combination with statistical and systematic error analysis methods to address randomness.

CRediT authorship contribution statement

Hong Tang: Writing – review & editing, Writing – original draft, Visualization, Methodology, Investigation, Funding acquisition, Formal analysis. **Alexander Melnikov:** Supervision, Data curation. **MingRui Liu:** Investigation, Formal analysis. **Stefano Sfarra:** Writing – review & editing, Investigation. **Hai Zhang:** Writing – review & editing, Supervision, Investigation, Funding acquisition. **Andreas Mandelis:** Writing – review & editing, Supervision, Project administration, Investigation, Funding acquisition.

Declaration of competing interest

The authors declare that they have no known competing financial interests or personal relationships that could have appeared to influence the work reported in this paper.

Acknowledgments

This work was supported in part by the National Key Research and Development Program of China (2023TFE0197800), National Natural Science Foundation of China (12402221) and Postdoctoral Fellowship Program of CPSF under Grant Number GZB20240962. The research was also supported by the Natural Sciences and Engineering Research Council of Canada Discovery Grants Program (RGPIN-2020–04595), the Canada Foundation for Innovation Research Chairs Program and the CFI-JELF program (38794).

Data availability

Data will be made available on request.

References

[1] I. Jenkins, Powder metallurgy, Nature 175 (1955) 276–279. Feb.
[2] G. Zhang, Y. Zhang, L. Zheng, Z. Peng, Research progress in powder metallurgy superalloys and manufacturing technologies for aero-engine application, Acta Metall. Sin. 55 (9) (2019) 1133–1144. Sep.
[3] Z. Tang, et al., Interface microstructure regulation and bonding performance of powder metallurgy Al/Mg bimetal with Ni interlayer, J. Mater. Sci. 58 (13) (2023) 5848–5864. Apr.
[4] R. Zhou, Z. Liu, J. Zhang, B. Liu, C. Du, Three-dimensional numerical simulation of green metal powder compacts crack based on DPC-CZM mixed model, Mater. Rep. 34 (6) (2020) 151–155.
[5] Persistence Market Research, Powder Metallurgy: Global Markets, BCC Publications, AVM007Q, May 2022. [Online]. Available: http://www.bccresearch.com/market-research/advanced-materials/powder-metallurgy-global-markets-to-markets-report.html.
[6] S. Benzerrouk, R. Ludwig, Infrared detection of defects in powder-metallic compacts, J. Nondestruct. Eval. 26 (1) (2007) 1–9. Mar.
[7] S. Benzerrouk, Active and passive thermography for the detection of defects in green-state powdermetallic compacts, ph.D. dissertation, Dept. Electr. Comput. Eng., Worcester Polytech. Inst., MA, USA, 2011.
[8] M.H. Rausch, K. Krzeminski, A. Leipertz, A.P. Fröba, A new guarded parallel-plate instrument for the measurement of the thermal conductivity of fluids and solids, Int. J. Heat. Mass Transf. 58 (1–2) (2013) 610–618. Mar.
[9] R.J. Warzoha, A.N. Smith, L. Boteler, A. Bajwa, Design considerations for miniaturized steady-state thermal characterization instruments, IEEE Trans. Compon. Pack. Manuf. Technol. 8 (8) (2018) 1401–1410. Aug.
[10] S. Chen, F. Zheng, C. Huang, Y. Zhang, Measurement of thermal diffusivity of thin film in thickness direction using an ordinary dielectric film as the sensor, IEEe Trans. Instrum. Meas. 71 (2022) 1–9. Mar.Art. no. 6001809.
[11] C. Huang, F. Zheng, S. Chen, Y. Zhang, Thermal diffusivity measurement in through-thickness direction of dielectric film with metal substrate, IEEE Trns. Dielectr. Electr. Insul. 29 (1) (2022) 38–46. Feb.
[12] C. Meola, Nondestructive evaluation of materials with rear heating lock-in thermography, IEEE Sens. J. 7 (10) (2007) 1388–1389. Sep.
[13] T. Aujeszky, G. Korres, M. Eid, Measurement-based thermal modeling using laser thermography, IEEE Trans. Instrum. Meas. 67 (6) (2018) 1359–1369. Jun.
[14] M.N. Özişik, Boundary Value Problems of Heat Conduction, Dover, New York, NY, USA, 1968, pp. 67–69.
[15] H.S. Carslaw, J.C. Jaeger, Conduction of Heat in Solids, 2nd ed., Clarendon Press, Oxford, UK, 1959, pp. 38–41.
[16] D.M. He, M.Q. Zheng, D.Z. Zhu, Z.Y. Guo, Measuring local heat transfer coefficientby infrared thermal wave imaging, J. Astr. Metr. Meas. 16 (2) (1996) 30–35. Apr.
[17] A. Mandelis, L. Nicolaides, Y. Chen, Structure and the reflectionless/refractionless nature of parabolic diffusion-wave fields, Phys. Rev. Lett. 87 (2) (2001). Jul.Art. no. 020801.
[18] A. Mandelis, Diffusion-Wave Fields: Mathematical Methods and Green functions, Springer, New York, NY, USA, 2001, pp. 101–105.
[19] C. Glorieux, J. Thoen, J. Fivez, Depth profiling of thermally inhomogeneous materials by neural network recognition of photothermal time domain data, J. Appl. Phys. 85 (10) (1999) 7059–7063. May.
[20] H. Tang, A. Melnikov, A. Mandelis, Deep learning neural network approach to thermal-wave imaging of damage in solids with application to diffusivity measurements of a green (unsintered) metal powder compact slab, Measurement 235 (2024). Aug.Art. no. 115004.
[21] R. Voti, C. Sibilia, M. Bertolotti, Photothermal depth profiling by genetic algorithms and thermal wave backscattering, Int. J. Thermophys. 26 (6) (2005) 1833–1848. Nov.
[22] M. Raissi, P. Perdikaris, G.E. Karniadakis, Physics-informed neural networks: a deep learning framework for solving forward and inverse problems involving nonlinear partial differential equations, J. Comput. Phys. 378 (2019) 686–707. Feb.
[23] L. Lu, X. Meng, Z. Mao, G.E. Karniadakis, DeepXDE: a deep learning library for solving differential equations, SIAM Rev. 63 (1) (2021) 208–228. Feb.

[24] S. Manavi, T. Becker, E. Fattahi, Enhanced surrogate modelling of heat conduction problems using physics-informed neural network framework, Int. Commun. Heat Mass 142 (2023). Mar.Art. no. 106662.
[25] S. Manavi, E. Fattahi, T. Becker, A parameterized physics-informed machine learning approach for solving heat and mass transfer equations in the drying process, Int. Commun. Heat Mass 158 (2024). Nov.Art. no. 107897.
[26] H. Tang, A. Melnikov, A. Mandelis, K. Sivagurunathan, Quantitative thermal-wave depth profiles of solids with spatially variant cooling coefficients imaged using lock-in thermography, Infrared Phys. Technol. 131 (2023). Jun.Art. no. 104669.
[27] J. Hua, Y. Li, C. Liu, P. Wan, X. Liu, Physics-informed neural networks with weighted losses by uncertainty evaluation for accurate and stable prediction of manufacturing systems, IEEE Trans. Neural Netw. Learn. Syst. 35 (8) (2024) 11064–11076. Aug.
[28] J. Tu, C. Liu, P. Qi, Physics-informed neural network integrating PointNet-based adaptive refinement for investigating crack propagation in industrial applications, IEEE Trans. Ind. Inform. 19 (2) (2023) 2210–2218. Feb.
[29] Z. Fang, A high-efficient hybrid physics-informed neural networks based on convolutional neural network, IEEE Trans. Neural Netw. Learn. Syst. 33 (10) (2022) 5514–5526. Oct.
[30] T. Kapoor, H. Wang, A. Núnez, R. Dollevoet, Physics-informed neural networks for solving forward and inverse problems in complex beam systems, IEEE Trans. Neural Netw. Learn. Syst. 35 (5) (2023) 5981–5995. Sep.
[31] M. Ryu, J.C. Batsale, J. Morikawa, Quadrupole modelling of dual lock-in method for the simultaneous measurements of thermal diffusivity and thermal effusivity, Int. J. Heat. Mass Transf. 162 (2020). Dec.Art. no. 120337.
[32] T. Ishizaki, et al., Measurement of thermal diffusivity distribution for murray and murchison meteorites using lock-in thermography, Int. J. Thermophys. 43 (7) (2022) 97–101. Jul.Art. no. 97.
[33] J.A. Dobrosotskaya, A.L. Bertozzi, A wavelet-laplace variational technique for image deconvolution and inpainting, IEEE Trans. Image Process. 17 (5) (2008) 657–663. May.
[34] T. Zhu, A new approach to active power calculation using wavelet coefficients, IEEE Trans. Power. Syst. 21 (2006) 435–437, no.1Feb.
[35] I. Daubechies, Ten lectures on wavelets, CBMS-NSF regional conference series in applied mathematics, Philadelphia, PA: SIAM Ed, 1992.
[36] K. Sebastian, A. Melnikov, K. Sivagurunathan, X. Guo, Wang X, A. Mandelis, Non-destructive lock-in thermography of green powder metallurgy component inhomogeneities: a predictive imaging method for manufactured component flaw prevention, NDT e Int. 127 (2022). Apr.Art. no. 102603.
[37] S.S. Pawar, V.P. Vavilov, Applying the heat conduction-based 3D normalization and thermal tomography to pulsed infrared thermography for defect characterization in composite materials, Int. J. Heat. Mass Transf. 94 (2016) 56–65. Mar.
[38] J.F. Florez-Ospina, H.D. Benitez, From local to global analysis of defect detectability in infrared non-destructive testing, Infrared Phys. Technol. 63 (2014) 211–221. Mar.
[39] G. Xavier, Y. Bengio, Understanding the difficulty of training deep feedforward neural networks, in: Proceedings of the 13th International Conference on Artificial Intelligence and Statistics, Sardinia, Italy, 2010, pp. 249–256, vol. 9 of Proc. Mach. Learn. Res.
[40] E. Kharazmi, Z. Zhang, and G. Karniadakis, Variational physics-informed neural networks for solving partial differential equations, 2019, arXiv:1912.00873.
[41] D.P. Kingma and J. Ba, Adam: a method for stochastic optimization, 2014, arXiv: 1412.6980.
[42] O. Kahveci, E. Cadirli, M. Ari, H. Tecer, M. Gündüz, Measurement and prediction of the thermal and electrical conductivity of Al-Zr overhead line conductors at elevated temperatures, Mater. Res. Ibero-am. J. Mater. 22 (1) (2019).
[43] M. Rombouts, L. Froyen, A.V. Gusarov, E.H. Bentefour, C. Glorieux, Photopyroelectric measurement of thermal conductivity of metallic powders, J. Appl. Phys. 97 (2) (2005). Jan.Art. no. 024905.
[44] H. Danninger, G. Leitner, Ch. Gierl-Mayer, Studying the progress of sintering in ferrous powder compacts by in-situ measuring the thermal conductivity, Powder Metall. Prog. 18 (2) (2018) 80–95. Dec.
[45] H. Bae, Y.C. Huang, O. Yang, P.H. Chou, B. Choi, Automated power control for mobile laser speckle imaging system, IEEE Embed. Syst. Lett. 1 (3) (2009) 73–76. Oct.